
Flexible ViG: Learning the Self-Saliency for Flexible Object Recognition

Lin Zuo, Kunshan Yang, Xianlong Tian,
Kunbin He, Yongqi Ding, Mengmeng Jing*
University of Electronic Science and Technology of China
linzuo@uestc.edu.cn,
{jingmeng1992, tianxianlong3, hekunbin19}@gmail.com
{ksyang, yqding}@std.uestc.edu.cn

Abstract

Existing computer vision methods mainly focus on the recognition of rigid objects, whereas the recognition of flexible objects remains unexplored. Recognizing flexible objects poses significant challenges due to their inherently diverse shapes and sizes, translucent attributes, ambiguous boundaries, and subtle inter-class differences. In this paper, we claim that these problems primarily arise from the lack of object saliency. To this end, we propose the Flexible Vision Graph Neural Network (FViG) to optimize the self-saliency and thereby improve the discrimination of the representations for flexible objects. Specifically, on one hand, we propose to maximize the channel-aware saliency by extracting the weight of neighboring nodes, which adapts to the shape and size variations in flexible objects. On the other hand, we maximize the spatial-aware saliency based on clustering to aggregate neighborhood information for the centroid nodes, which introduces local context information for the representation learning. To verify the performance of flexible objects recognition thoroughly, for the first time we propose the Flexible Dataset (FDA), which consists of various images of flexible objects collected from real-world scenarios or online. Extensive experiments evaluated on our Flexible Dataset demonstrate the effectiveness of our method on enhancing the discrimination of flexible objects.

1 Introduction

Computer vision [1; 2; 3; 4] has been widely employed in various applications, ranging from simple object recognition to complex scene understanding [5; 6]. Image recognition is categorized into two main types: rigid and non-rigid objects recognition. Rigid objects, as illustrated in Figure 1 (a), maintain consistent shapes and sizes regardless of their positioning or viewing angle. In the past decades, the recognition of rigid objects has been well explored and shown excellent performance due to their invariant geometrical structure and appearance property. Notably, the convolutional neural network could effectively extract the features of the rigid objects [1]. Non-rigid objects, however, exhibit inconsistent shapes or sizes, resulting in various appearances depending on their positions and viewing angles. Their variations in shape and size pose challenges in recognition. Flexible objects, a subset of non-rigid objects, show even larger variations in size and shape. As illustrated in Figure 1 (b), flexible objects, e.g., clouds, smoke, water, flames, and glare, not only vary greatly in shape and size but may be semi-transparent and lack clear boundaries [7], which makes it extremely difficult to extract discriminative representations. Furthermore, the small inter-class differences among flexible objects make them challenging to distinguish.

Recognizing flexible objects is critical in numerous application fields. For example, recognizing flames and smoke is vital for early fire detection [8], precise recognition of different cloud formations plays a key role in weather forecasting and climate monitoring [9], and accurate recognition of elements such as glare [10] is essential for achieving realism and visual coherence in composite imagery. Despite the importance of these tasks, a fundamental requirement for training effective

discriminative deep models is the availability of high-quality datasets. However, existing data sets dedicated to fire [11; 12] and cloud [13; 9] are narrowly focused on singular recognition tasks, thus demonstrating limited challenges and diversities. These datasets do not include various flexible objects, leading to models trained on them exhibiting diminished discriminative capabilities. To solve this problem, we propose the FDA dataset, specifically designed for flexible objects research. FDA comprises a diverse range of flexible objects images gathered from real-world scenarios and online resources, providing extensive training and testing data.

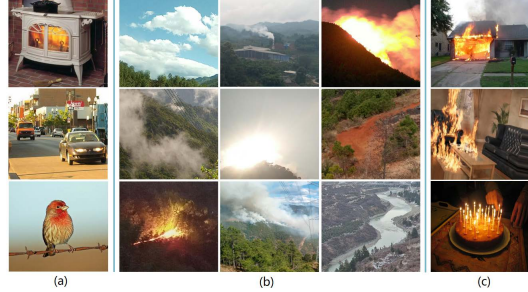


Figure 1: (a) rigid objects. (b) flexible objects images from our proposed FDA. (c) fire images from FireNet dataset.

Although several studies [11; 8] have attempted to recognize flexible objects, they typically focus on recognizing one or two specific types within images, not addressing the need for detailed differentiation and recognition of multiple categories of flexible objects. Two primary issues impede the recognition of flexible objects: firstly, the diversity and irregularity in their shapes and sizes, especially their translucent physical properties or unclear boundaries, hinder the extraction of consistent representational features; secondly, the small inter-class differences make them hard to distinguish. These issues stem from a lack of saliency in flexible objects. Saliency refers to the distinct and prominent features that make objects stand out from their surroundings and differentiate them from other categories of objects.

To mitigate these problems, we propose Flexible ViG in this paper, which is primarily optimized for saliency. Channel-aware saliency is employed to address the difficulty in extracting consistent representation caused by the diverse variations in the shape and size of flexible objects. Spatial-aware saliency is utilized to address the challenge of identifying flexible objects with minimal inter-class differences. By optimizing both channel and spatial aspects, Flexible ViG enhances the discrimination capabilities for flexible objects. Extensive experiments demonstrate the effectiveness of our FViG method in capturing neighboring relationship and enhancing the representation capacity of central nodes. The main contributions of this work are as follows.

- (1) We propose Flexible ViG, designed to maximize self-saliency. In which, channel-aware saliency adaptively captures neighboring relationships by extracting channel weight information, matching the various shapes and sizes of flexible objects. This improves the model’s sensitivity to fine-grained features, enhancing its ability to distinguish flexible objects from backgrounds. Spatial-aware saliency enhances node representation through node-level clustering, aggregating overlooked neighboring node information to update central nodes.
- (2) We have created a dataset named FDA, which consists of diverse images of flexible objects collected from real-world scenarios or online sources. To the best of our knowledge, FDA is the first extensive, multi-category dataset specifically designed for the recognition of flexible objects. This dataset establishes a benchmark for evaluating the performance of models in flexible objects recognition tasks.
- (3) Extensive experiments on the FDA dataset demonstrate the effectiveness of our proposed FViG, achieving recognition performance comparable to other state-of-the-art methods. Furthermore, these experiments validate that the FDA dataset serves as a reliable benchmark to evaluate the performance of various methods.

2 Related Work

2.1 Graph Neural Network

Graph Neural Networks (GNNs) [14; 15], Graph Convolutional Networks (GCNs) [16; 17], and Graph Attention Networks (GATs) [18; 19] have received significant attention in recent years for their ability to handle data with complex relationships and topological structures. These models excel in analyzing graph-structured data and are applied in diverse fields, including social networks, recommendation systems, and molecular chemistry. GNNs [15] focus on the acquisition of node representations through dynamic exchange and aggregation of information between nodes. The advent of GCNs [17] introduced the concept of convolution to structured non-Euclidean spaces. There are two primary types: spectral-based, which leverages Fourier transforms and graph signal processing through eigen decomposition; and spatial-based, which defines convolutions directly on the graph, updating the feature representations of central nodes via a message-passing mechanism. Velickovic et al. [18] introduced the GAT model, which incorporates attention mechanisms into GNN to dynamically weight the influence of neighboring nodes during the aggregation process, focusing on more significant nodes. However, these methods are primarily suited for structured data, such as in text processing, and are less effective for learning features with unstructured data such as images. In contrast, our FViG is capable of adapting to these unstructured images.

2.2 Graph Vision Model

Shen et al. [20] introduced the interactive graph transformer (GiT), designed for vehicle re-identification. Zheng et al. [21] developed a graph transformer network designed for whole-slide image representations, incorporating a novel transformer fusion method. Furthering the combination of graph convolution and self-attention, Lin et al. [22] presented Mesh Graphormer, a technique for reconstructing human poses and meshes from single images. Gu [19] introduced GANR, a network representation based on graph attention, which employs the attention mechanism to uncover and quantify the relationships and significance of the nodes, demonstrating superior performance in applications such as link prediction. Ma [23] explored the local structural details of the graphs through GAT and introduced GAT-POS, an enhancement to GAT that incorporates positional embeddings to represent the structural and positional data of the nodes. GAT-POS recorded remarkable results on heterogeneous graph-structured datasets. Marking a pioneering fusion of graph structures with images, Han et al. [24] proposed the Vision Graph Neural Network (ViG). This network treats each image patch as an individual graph node and utilizes a k-NN approach to establish relationships between these patches. Despite its innovative approach, ViG primarily captures image patch similarity, potentially overlooking the latent manifold structure of the image. Furthermore, the construction of graph structures is crucial, and Li [25] emphasized the importance of studying different distance metrics to build graph structures. However, ViG adopts the Euclidean distance to measure the dependencies between nodes for graph construction. This method could not adequately capture the complex geometric relationships between different patches [26; 27; 28; 29; 25; 14]. In contrast, we propose channel-aware saliency learning to adaptively capture neighboring relationships and learn fine-grained graph representations.

2.3 Clustering

Clustering constitutes an unsupervised learning algorithm characterized by the generation of clusters, each comprising a collection of data objects. Within these clusters, objects display pronounced intracluster similarity and markedly reduced intercluster similarity. A quintessential example of such algorithms is K-means, introduced by MacQueen [30]. This method seeks to determine k centroids within a dataset and to partition the dataset into k distinct clusters, with the objective of minimizing the sum of squared distances from each data point to its nearest centroid. CLARA [31] strategically extracts a subset of data points as a representative sample from the dataset, subsequently employing the Partitioning Around Medoids (PAM) algorithm on this sample to improve computational efficiency. Furthermore, Affinity propagation clustering, pioneered by Frey et al. [32] is recognized as a rapid and effective clustering algorithm.

Both Vision GNN [24] and deepGCN [25] employ dilated graph convolutions, which significantly expand the receptive field, address oversmoothing issues during model training, and improve graph representation capabilities. However, these methods do not fully utilize the information from the

nodes in dilated regions. Such neglected nodes are critical for graph representation learning. Inspired by Ma’s proposed method of patch-level aggregation and dispatch [33], we propose spatial-aware saliency learning based on node-level feature clustering to effectively establish graph learning relationships among nodes within dilated regions, thereby enhancing the overall model’s learning and representation capacity.

3 Method

Saliency refers to the distinct and prominent features that enable objects to stand out from their surroundings and facilitate differentiation from other object categories. Subsequently, as shown in Figure 2, we optimize saliency from both channel-aware and spatial-aware aspects.

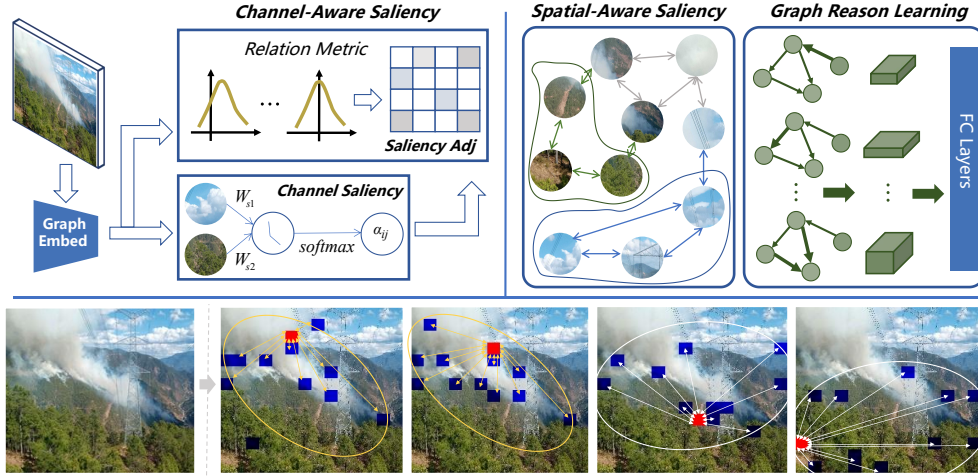


Figure 2: The top section describes the workflow of the proposed FViG, encompassing graph embedding, relation metrics, graph attention, graph generation and clustering, and graph reasoning learning. The bottom section details the graph construction process, with red blocks indicating central nodes and blue blocks indicating adjacent nodes. By selecting and clustering central nodes and their adjacent nodes, the model captures discriminative features and manifold structures within the image, thus improving the accuracy of flexible objects recognition.

3.1 Learning of Channel-Aware Saliency

Flexible objects exhibit more diverse variations in shape and size, which pose challenges to representation learning. To tackle this, we optimize channel-aware saliency based on attention-driven graph construction, which dynamically captures node relationships by extracting the weight saliency information from each channel, corresponding to the varied shapes and sizes of flexible objects. Furthermore, the model’s ability to detect fine-grained features is specifically improved, enabling it to more efficiently distinguish flexible objects from their backgrounds.

We divide an image into N patches and utilize graph embedding to associate them with node vectors $V = [v_1, v_2, \dots, v_N] \in \mathbb{R}^{B \times N \times D}$, where B is batchsize and D denotes feature dimensions. For each node v_i within the graph, we compute the Euclidean distance to identify the k nearest neighbor nodes, collectively denoted as $\mathcal{N}(v_i) \in \mathbb{R}^{B \times K \times D}$. For each neighboring node v_j , we establish an edge e_{ij} connecting it to v_i . By traversing all nodes, the set of edges E is obtained. Consequently, we can construct the graph as $G = (V, E)$.

To improve comprehension of intrinsic nodes relationships of vectors $V \in \mathbb{R}^{B \times N \times D}$, we map these D -dimensional features to a D' -dimensional linear latent space via a trainable matrix $\mathbf{W} \in \mathbb{R}^{D \times D'}$, and the transformed node vectors $V' \in \mathbb{R}^{B \times N \times D'}$ is obtained.

$$V' = V \cdot W \quad (1)$$

In addition, we define a learnable vector $W_s = [W_{s1} || W_{s2}] \in \mathbb{R}^{2D \times 1}$ to project the node feature vectors V into the attention space to calculate the saliency score, where $||$ denotes as concatenate

operation, $W_{s1} \in \mathbb{R}^{D \times 1}$ means the feature projection matrix of the node itself, and $W_{s2} \in \mathbb{R}^{D \times 1}$ represents the feature projection matrix of each node with respect to all other nodes. So, we can compute the saliency relationships among nodes:

$$\begin{cases} S_s = V' \cdot W_{s1} \\ S_n = (V' \cdot W_{s2})^T \end{cases}, \quad (2)$$

where $S_s \in \mathbb{R}^{B \times N \times 1}$ denotes saliceny score of the N nodes itself, $S_n \in \mathbb{R}^{B \times 1 \times N}$ denotes saliceny score of each central node versus all N neighboring nodes. Then, we calculate the attention between nodes saliency score S_s and S_n by broadcast addition, gaining the saliency attention matrix $S \in \mathbb{R}^{B \times N \times N}$:

$$S = \begin{bmatrix} S_{s1} \\ S_{s2} \\ \vdots \\ S_{sN} \end{bmatrix} + [S_{n1} \quad S_{n2} \quad \cdots \quad S_{nN}] = \begin{bmatrix} S_{s1} + S_{n1} & S_{s1} + S_{n2} & \cdots & S_{s1} + S_{nN} \\ S_{s2} + S_{n1} & S_{s2} + S_{n2} & \cdots & S_{s2} + S_{nN} \\ \vdots & \vdots & \ddots & \vdots \\ S_{sN} + S_{n1} & S_{sN} + S_{n2} & \cdots & S_{sN} + S_{nN} \end{bmatrix}. \quad (3)$$

Since W_{s1} and W_{s2} are learnable, saliency attention S is capable of adaptively capturing the weight information of the feature channels. Each element s_{ij} in matrix S denotes the attention score between node i and j . Additionally, we apply normlization methods to obtain the weighted saliceny attention matrix between nodes:

$$\alpha_{ij} = \text{softmax}(s_{ij}) = \frac{\exp(s_{ij})}{\sum_{k \in \mathcal{N}_i} \exp(s_{ik})}. \quad (4)$$

Otherwise, α_{ij} is transformed by the non-linear LeakyReLU activation function to improve feature diversity, we can obtain:

$$\alpha_{ij} = \frac{\exp(\text{LeakyReLU}(s_{ij}))}{\sum_{k \in \mathcal{N}_i} \exp(\text{LeakyReLU}(s_{ik}))} \quad (5)$$

Reviewing the graph construction methodology for ViG, we initially compute the Euclidean distance between all nodes, which forms the node distance matrix $eudist$. Subsequently, we apply the k -nearest neighbors (KNN) algorithm to determine the k -nearest nodes, leading to the creation of the adjacency matrix:

$$Adj = Top - k(eudist, k), \quad (6)$$

using the saliency attention derived from Equation 5, we develop a trainable distance metric $\alpha_{ij} * (-eudist)$ that relies on the node relationships e_{ij} . As a result, we generate an adaptive adjacency matrix based on saliency attention :

$$saliencyAdj = Top - k(\alpha_{ij} * eudist, k). \quad (7)$$

3.2 Learning of Spatial-Aware Saliency

Recognizing flexible objects presents a significant challenge due to the minimal differences between classes, which makes them difficult to distinguish. In response, we optimize spatial-aware saliency based on node-level clustering designed to harness underexploited information from nodes within dilated neighboring areas to enhance central nodes. This method promotes interactions within the local context, thus enhancing discrimination capabilities and ensuring better distinction between different categories of flexible objects.

For each central node $v_i, (i = 1, 2, \dots, N)$ and its neighboring node $v_j \in \mathcal{N}(v_i)$, in order to fully leverage the dilated information, we employ all k neighboring nodes of v_i to fuse the node information of $\mathcal{N}(v_i)$ using clustering methods; Then, we define a cluster center c_i for $\mathcal{N}(v_i)$ by performing average pooling, and node feature similarity s_j is obtained between c_i and v_j based on cosine similarity calculation. Consequently, we obtain the clustered node representation as follows:

$$C_f = \frac{1}{\lambda} \left(c_i + \sum_{j=1}^k \sigma(\alpha s_j + \beta) * v_j \right) \lambda = 1 + \sum_{j=1}^k \sigma(\alpha s_j + \beta), \quad (8)$$

where α and β are learnable parameters that enable s_j to adaptively change, and λ is a regularization term. To maintain adequate representational capabilities, it is essential to incorporate at least one

learnable linear transformation to convert the input node features into higher-order features. A 1×1 convolution is employed for feature mapping by Coc [33], yet this method notably increases the computational complexity. Consequently, we utilize a learnable linear transformation matrix $W \in \mathbb{R}^{D' \times D}$ to facilitate dimension transformation of the initial node feature vectors, thereby diminishing computational overhead. Furthermore, we implement multiple heads, numbered at M , to improve the clustering effect. Thus, we obtain:

$$C'_f = \prod_{m=1}^M \frac{1}{\lambda} \left(W \cdot c_i^m + \sum_{j=1}^k \sigma(\alpha s_j^m + \beta) * (W \cdot \nu_j^m) \right), \quad (9)$$

subsequently, the clustered features C'_f are adaptively allocated to each node within the cluster according to their similarity. These nodes communicate with each other and share the features among them within the cluster. A linear transformation matrix $W' \in \mathbb{R}^{D \times D'}$ is adopted, and for each node ν_j , the following update is applied:

$$\nu'_j = \nu_j + W' \cdot (\sigma(\alpha s_j + \beta) * C'_f). \quad (10)$$

3.3 Graph Reason Learning

Previously, we effectively clustered information from adjacent nodes. In this section, we explore the learning interactions between central nodes and their adjacent nodes within the graph. This involves facilitating the learning of node features through processes of aggregation and updating. The process of learning node representations is described as follows:

$$G' = Update(Aggregate(G, W_{agg}), W_{update}), \quad (11)$$

where G is the graph built on the clustered feature C'_f , W_{agg} and W_{update} are the parameters for aggregation and updating, respectively. The graph convolution consists of l layers (In this paper, setting $l = 12$.), and the outputs of the upper layers serve as inputs to the lower layers through stacking. Finally, to increase the diversity of features, we utilize a feed-forward neural network (FFN) to map the node features.

4 FLEXIBLE DATASET

The advancement of discriminative deep learning models is crucially dependent on the access to high-quality datasets. Datasets designed for particular recognition tasks such as fire [11; 12] and cloud [13; 9] are often narrowly focused, offering limited diversity and challenges. To address these constraints, we propose the FDA—a publicly available, high-quality dataset that includes a wide variety of flexible objects. The FDA are able to be downloaded for research purposes through this access link.

Table 1: Statistics on FireNet Dataset

| Categorize | Train | Test |
|------------|-------|------|
| Fire | 1124 | 593 |
| NoFire | 1301 | 278 |
| total | 2425 | 871 |

4.1 FireNet Dataset

Jadon et al. [11] have constructed a flame dataset for training fire detection models [11], comprising 3,296 images. This dataset is divided into two categories: images that contain fire and those without. Table 1 shows the specific details of the image distribution within these categories for both training and test sets. The majority of the FireNet images, sourced online, are solely focused on detecting flames and do not incorporate other variable objects, thus reducing the dataset’s realism and diversity. Furthermore, as illustrated in Figure 1 (c), fires are generally captured from a close distance with clear fire characteristics, simplifying the detection process and allowing a lightweight convolutional neural network to achieve accuracies exceeding 90%.

4.2 Our FDA Dataset

Comparable in scale to the FireNet dataset [11], our FDA is carefully selected based on the unique characteristics of flexible objects. Specifically, we gathered 2,080 images of flexible objects from real-world scenarios, organizing them into nine fine-grained categories: cloud, facsmoke, fire, fog, glare, ground, light, smoke and water. Additionally, we supplemented this collection with nearly ten thousand images sourced from the Internet, including not only flexible objects but also animals, humans, and vehicles, thus enhancing the diversity of instance. From this extensive collection, we handpicked 394 challenging images to enrich our dataset, thus creating a more diverse and realistic repository. Our flexible objects samples were deliberately chosen for their varying degrees of transparency, shapes, and sizes to highlight their complexity and diversity. Each sample was precisely categorized to ensure accuracy in classification. The final dataset contains 2,474 images,

with detailed descriptions of each category presented in Table 2. Figure 1(b) presents several FDA example images, providing an overview of the entire flexible objects dataset. In contrast to the FireNet dataset, our images are primarily sourced from real-world scenarios and range from close-up to distant perspectives. The flexible objects exhibit common characteristics, such as variable sizes, shapes, and semitransparency. However, they also display unique traits that contribute to their complexity. This diversity not only poses significant challenges for the recognition of flexible objects, but also establishes an effective benchmark for evaluating methods of flexible objects recognition.

Table 2: Statistics on our FDA

| Categorize | Real-World | Online |
|------------|------------|--------|
| cloud | 201 | 69 |
| facsmoke | 68 | 41 |
| fire | 422 | 39 |
| fog | 262 | 66 |
| glare | 98 | 25 |
| ground | 206 | 42 |
| light | 109 | 25 |
| smoke | 437 | 54 |
| water | 277 | 33 |
| total | 2080 | 394 |

5 Experiments

In this section, extensive experiments are performed to confirm the challenge of the proposed FDA and the performance of FViG. Comprehensive details of these experiments are included in the Appendix.

Table 3: Comparison results of FViG with current SOTA models on FDA

| Category | Method | Parameters(M) | Computation(G) | Accuracy(%) |
|-------------|-----------------------|---------------|----------------|--------------|
| Transformer | ViT-B/16 [4] | 86.8 | 17.6 | 76.38 |
| | T2T-ViT-14 [34] | 21.5 | 4.8 | 75.46 |
| | DaViT-Small [35] | 49.7 | 8.8 | 77.19 |
| | DeiT-S [36] | 22.1 | 4.6 | 78.82 |
| | Swin-S [37] | 50 | 8.7 | 78.58 |
| | Twins-SVT-S [38] | 24 | 2.9 | 30.32 |
| CNN | Resnet50 [1] | 25.6 | 4.1 | 70.37 |
| | Resnet101 [1] | 45 | 7.9 | 72.18 |
| | Regnet [39] | 4.78 | 0.406 | 74.65 |
| | Densenet [40] | 18 | 4.37 | 71.29 |
| MLP | Mlp-mixer-base [41] | 59 | 12.7 | 68.76 |
| | Mlp-mixer-larger [41] | 207 | 44.8 | 68.17 |
| Graph | Vig-s [24] | 22.7 | 4.5 | 74.68 |
| | Vig-ti [24] | 7.1 | 1.3 | 75.37 |
| | Coc-tiny [33] | 5.3 | 1 | 77.08 |
| | Coc-small [33] | 14 | 2.6 | 81.41 |
| | FViG | 21.16 | 4.35 | 80.72 |
| | FViG-tiny | 5.98 | 1.23 | 78.10 |

5.1 Comparison with SOTA Models

We conducted a comprehensive experimental evaluation on the FDA dataset to substantiate the improved performance of our FViG compared to current SOTA models. As detailed in Table 3,

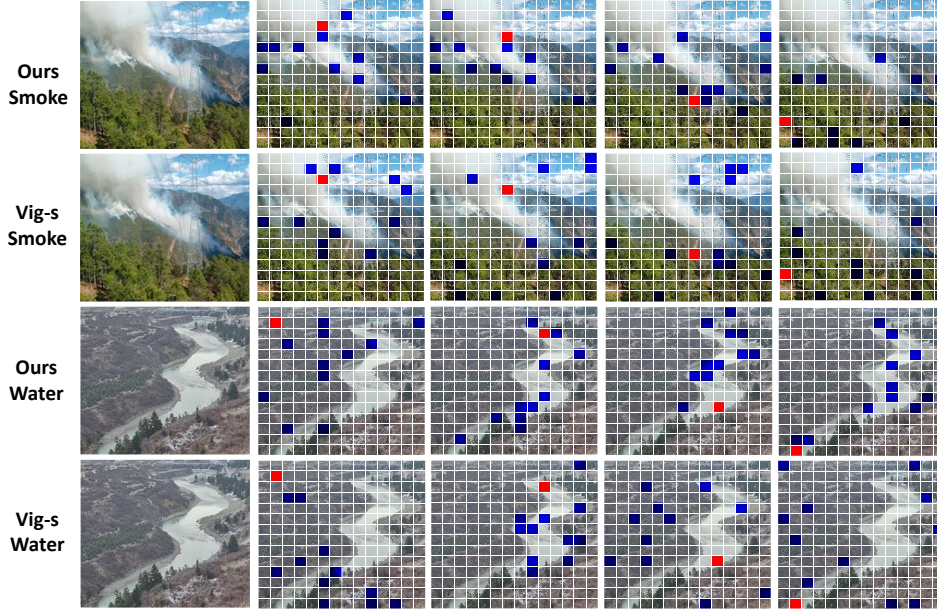


Figure 3: Visualization of the constructed graph structure. For the images of smoke and water, we selected two central nodes from both the foreground and background. The patches represented by these chosen nodes are marked in red, and the nodes that eventually form neighboring relationships with them are marked in blue.

these comparative experiments were rigorously designed to assess the efficacy of the proposed FViG against an array of established models, including those based on Transformers, Convolutional Neural Networks (CNNs), Multilayer Perceptrons (MLPs) and various GNNs. Our FViG and its compact variant, FViG-tiny, showcased in bold, exhibit an impressive balance of parameter efficiency, computational cost, and predictive accuracy. Remarkably, FViG achieves an accuracy of 80.72%, which is significantly better than traditional CNN and MLP, as well as the other GNN models. Impressively, it achieves this superior accuracy with a reduced parameter count of 21.16 million, which is less than quarter compared to certain Transformer models such as ViT-B/16. Additionally, the computational cost of FViG, at 4.35 Gflops, is relatively low, demonstrating its efficiency, particularly when compared with the MLP-mixer-large model that requires a significant computational overhead of 44.8 Gflops. The tiny version of FViG further emphasizes efficiency, requiring only 5.98 million parameters and 1.23 Gflops, while still achieving a commendable accuracy of 78.10%. Furthermore, the detailed experiment conducted on the FireNet dataset can be found in Appendix A.3.

This variant offers a viable alternative for scenarios with constrained computational resources that maintain high performance without considerable sacrifice. Our models, which stand out by their innovative architectural design, excel not only in diminishing computational demands but also in augmenting the accuracy of flexible objects recognition. This highlights the effectiveness of our method in addressing the complexities and challenges associated with flexible objects recognition.

Table 4: Ablation results of our FViG with various configurations.

| Baseline | Channel Saliency | Spatial Saliency | Dilation | Accuracy(%) |
|----------|------------------|------------------|----------|--------------|
| ✓ | | | | 74.68 |
| ✓ | ✓ | | | 77.3(↑2.62) |
| ✓ | | ✓ | | 78.9(↑4.22) |
| ✓ | ✓ | ✓ | | 79.13(↑4.45) |
| ✓ | | ✓ | ✓ | 79.01(↑4.33) |
| ✓ | ✓ | ✓ | ✓ | 80.72(↑6.04) |

5.2 Ablation Study

We analyze each part of the model to determine their individual contributions to the overall performance. Table 4 in our study presents various configurations of our method along with their corresponding accuracy. The baseline ViG achieved an accuracy of 74.68%. The introduction of

channel-aware saliency module resulted in a 2.62% increase in accuracy, indicating that saliency attention could improve the model sensitivity to distinguish flexible objects. The introduction of the spatial-aware saliency module resulted in a 4.22% increase in accuracy, indicating that the Cluster is able to facilitate interaction in the local context and improve discrimination ability. The introduction of channel-aware and spatial-aware saliency modules led to a substantial performance increase, with an accuracy of 79.13%. The adoption of the spatial-aware saliency and Dilation modules resulted in a 4.33% increase in accuracy, indicating that the Dilation module could enhance the feature of central nodes by establishing graph relationships between nodes within dilated regions. Ultimately, when all modules were incorporated, our method achieved an accuracy of 80.72%.

5.3 Visualization

To better understand the workings of our FViG, we visualized the graph structure constructed within the FViG and compared it with the ViG model. In Figure 3, we illustrate the differences in graph structure when using the FViG and ViG models for two different categories of input samples (smoke and water). For the images of smoke and water, we selected two central nodes in both the foreground and background, respectively. The patches corresponding to these nodes are colored red, whereas the nodes that subsequently establish neighboring relationships are colored blue. We observed that when the patch of a chosen central node represents the foreground, the FViG tends to select neighboring nodes primarily from the foreground. Conversely, when the central node’s patch represents the background, the neighboring nodes chosen are mostly from the background. But ViG’s performance is much worse, whether the central node is foreground or background. Our model is more capable of selecting neighboring nodes relevant to the current node’s content and is more effective in recognizing flexible objects.

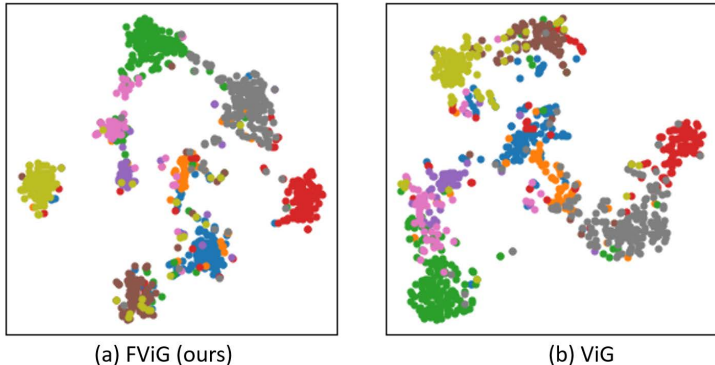


Figure 4: A comparative study of t-SNE visualizations is conducted for our FViG and ViG.

5.4 t-SNE Analysis

As illustrated in Figure 4 (a) and Figure 4 (b), we present the t-SNE visualization for FViG and ViG, respectively. In these visualizations, the clustering achieved by FViG appears more cohesive, with clearer demarcations among categories. The vividly colored clusters are well-separated, demonstrating the effectiveness of our method in distinguishing these data points. Additionally, FViG shows fewer outliers, suggesting a higher resilience in handling noise or outliers. In contrast, the clusters in ViG are less distinct, with some colored clusters (such as red and blue) positioned closely, and certain areas exhibiting blurred boundaries. Moreover, ViG displays a greater number of outliers and more dispersed clusters, indicating a potential weakness in dealing with datasets that have indistinct boundaries.

6 Conclusion

In this paper, we have constructed a diverse dataset and proposed the Flexible Vision Graph Network (FViG) for the recognition of flexible objects. We address the major challenges in flexible objects recognition by employing channel-aware saliency learning to enable the adaptation of graph representation and spatial-aware saliency learning to improve the discriminative capabilities, respectively.

Extensive experiments on the FDA and FireNet datasets demonstrate the effectiveness of our proposed FViG, achieving recognition performance comparable to other SOTA methods. Our study indicates the efficacy of FViG in fine-grained and irregular features of flexible objects. Despite its advantages, while FViG performs well on datasets specifically curated for flexible objects, its generalizability to other domains or more diverse datasets remains to be thoroughly investigated.

References

- [1] Kaiming He, Xiangyu Zhang, Shaoqing Ren, and Jian Sun. Deep residual learning for image recognition. In *Proceedings of the IEEE conference on computer vision and pattern recognition*, pages 770–778, 2016.
- [2] Ashish Vaswani, Noam Shazeer, Niki Parmar, et al. Attention is all you need. *Advances in Neural Information Processing Systems*, 30, 2017.
- [3] Nicolas Carion, Francisco Massa, Gabriel Synnaeve, Nicolas Usunier, Alexander Kirillov, and Sergey Zagoruyko. End-to-end object detection with transformers. In *European conference on computer vision*, pages 213–229. Springer, 2020.
- [4] Alexey Dosovitskiy et al. An image is worth 16x16 words: Transformers for image recognition at scale. *arXiv preprint arXiv:2010.11929*, 2020.
- [5] Risto Miikkulainen, Jason Liang, Elliot Meyerson, Aditya Rawal, Dan Fink, Olivier Francon, Bala Raju, Hormoz Shahrzad, Arshak Navruzyan, Nigel Duffy, et al. Evolving deep neural networks. In *Artificial intelligence in the age of neural networks and brain computing*, pages 269–287. Elsevier, 2024.
- [6] Paria Mehrani and John K Tsotsos. Self-attention in vision transformers performs perceptual grouping, not attention. *Frontiers in Computer Science*, 5:1178450, 2023.
- [7] Manorama Jha. Point cloud registration of non-rigid objects in sparse 3d scans with applications in mixed reality. *arXiv preprint arXiv:2212.03856*, 2022.
- [8] Haifeng Wang, Yi Zhang, and Xin Fan. Rapid early fire smoke detection system using slope fitting in video image histogram. *Fire technology*, 56(2):695–714, 2020.
- [9] Jiancheng Zhang, Ping Liu, Fan Zhang, and Qian Song. Cloudnet: Ground-based cloud classification with deep convolutional neural network. *Geophysical Research Letters*, 45(16):8665–8672, 2018.
- [10] Yicheng Wu, Qirui He, Tianfan Xue, Rahul Garg, Jiawen Chen, Ashok Veeraraghavan, and Jonathan T Barron. How to train neural networks for flare removal. In *Proceedings of the IEEE/CVF International Conference on Computer Vision*, pages 2239–2247, 2021.
- [11] Arpit Jadon, Mohd Omama, Akshay Varshney, Mohammad Samar Ansari, and Rishabh Sharma. Firenet: a specialized lightweight fire & smoke detection model for real-time iot applications. *arXiv preprint arXiv:1905.11922*, 2019.
- [12] Pasquale Foggia, Alessia Saggese, and Mario Vento. Real-time fire detection for video-surveillance applications using a combination of experts based on color, shape, and motion. *IEEE TRANSACTIONS on circuits and systems for video technology*, 25(9):1545–1556, 2015.
- [13] Alex Krizhevsky, Geoffrey Hinton, et al. Learning multiple layers of features from tiny images. 2009.
- [14] Daniel Carlos Guimaraes Pedronette, Otávio AB Penatti, and Ricardo da S Torres. Unsupervised manifold learning using reciprocal knn graphs in image re-ranking and rank aggregation tasks. *Image and Vision Computing*, 32(2):120–130, 2014.
- [15] Lilapati Waikhom and Ripon Patgiri. Graph neural networks: Methods, applications, and opportunities. *arXiv preprint arXiv:2108.10733*, 2021.
- [16] Shirui Zhang, Hanghang Tong, Jie Xu, and Ross Maciejewski. Graph convolutional networks: A comprehensive review. *Computational Social Networks*, 6(1):1–23, 2019.

- [17] Thomas N Kipf and Max Welling. Semi-supervised classification with graph convolutional networks. *arXiv preprint arXiv:1609.02907*, 2016.
- [18] Petar Veličković, Guillem Cucurull, Arantxa Casanova, Adriana Romero, Pietro Lio, and Yoshua Bengio. Graph attention networks. *arXiv preprint arXiv:1710.10903*, 2017.
- [19] Weiwei Gu, Fei Gao, Xiaodan Lou, and Jiang Zhang. Discovering latent node information by graph attention network. *Scientific Reports*, 11(1):6967, 2021.
- [20] Fei Shen, Yi Xie, Jianqing Zhu, Xiaobin Zhu, and Huanqiang Zeng. Git: Graph interactive transformer for vehicle re-identification. *IEEE Transactions on Image Processing*, 32:1039–1051, 2023.
- [21] Seongjun Yun, Minbyul Jeong, Sungdong Yoo, Seunghun Lee, S Yi Sean, Raehyun Kim, Jaewoo Kang, and Hyunwoo J Kim. Graph transformer networks: Learning meta-path graphs to improve gnns. *Neural Networks*, 153:104–119, 2022.
- [22] Kevin Lin, Lijuan Wang, and Zicheng Liu. Mesh graphormer. In *Proceedings of the IEEE/CVF international conference on computer vision*, pages 12939–12948, 2021.
- [23] Liheng Ma, Reihaneh Rabbany, and Adriana Romero-Soriano. Graph attention networks with positional embeddings. In *Pacific-Asia Conference on Knowledge Discovery and Data Mining*, pages 514–527. Springer, 2021.
- [24] Kai Han, Yunhe Wang, Jianyuan Guo, Yehui Tang, and Enhua Wu. Vision gnn: An image is worth graph of nodes. *Advances in neural information processing systems*, 35:8291–8303, 2022.
- [25] Guohao Li, Matthias Muller, Ali Thabet, and Bernard Ghanem. Deepgcns: Can gcns go as deep as cnns? In *Proceedings of the IEEE/CVF international conference on computer vision*, pages 9267–9276, 2019.
- [26] Jingqin Lv, Jiangxiong Fang, et al. A color distance model based on visual recognition. *Mathematical Problems in Engineering*, 2018, 2018.
- [27] Haibin Ling and David W Jacobs. Shape classification using the inner-distance. *IEEE transactions on pattern analysis and machine intelligence*, 29(2):286–299, 2007.
- [28] Nikita Lomov. Skeleton-geodesic distances for shape recognition: Efficient computation by continuous skeleton. In *VISIGRAPP (4: VISAPP)*, pages 307–314, 2020.
- [29] HyeongJin Kim, GyungHyun Lee, and Byoung Chul Ko. Vit graph head attention for small sized datasets. In *Workshop on Efficient Systems for Foundation Models@ ICML2023*, 2023.
- [30] James MacQueen et al. Some methods for classification and analysis of multivariate observations. In *Proceedings of the fifth Berkeley symposium on mathematical statistics and probability*, volume 1, pages 281–297. Oakland, CA, USA, 1967.
- [31] Erich Schubert and Peter J. Rousseeuw. Faster k-medoids clustering: Improving the pam, clara, and clarans algorithms. In *Similarity Search and Applications*, pages 171–187. Springer International Publishing, 2019.
- [32] Brendan J Frey and Delbert Dueck. Clustering by passing messages between data points. *science*, 315(5814):972–976, 2007.
- [33] Xiang Ma, Yongchao Zhou, Hang Wang, Cheng Qin, Bo Sun, Chuan Liu, and Yanwei Fu. Image as set of points. *arXiv preprint arXiv:2303.01494*, 2023.
- [34] Li Yuan et al. Tokens-to-token vit: Training vision transformers from scratch on imagenet. In *Proceedings of the IEEE/CVF International Conference on Computer Vision*, pages 558–567, 2021.
- [35] Mingyu Ding, Bin Xiao, Noel Codella, Ping Luo, Jingdong Wang, and Lu Yuan. Davit: Dual attention vision transformers. In *European conference on computer vision*, pages 74–92. Springer, 2022.

- [36] Hugo Touvron et al. Training data-efficient image transformers & distillation through attention. In *International Conference on Machine Learning*, pages 10347–10357. PMLR, 2021.
- [37] Ze Liu, Yutong Lin, Yue Cao, Han Hu, Yixuan Wei, Zheng Zhang, Stephen Lin, and Baining Guo. Swin transformer: Hierarchical vision transformer using shifted windows. In *Proceedings of the IEEE/CVF international conference on computer vision*, pages 10012–10022, 2021.
- [38] Xiangxiang Chu, Zhi Tian, Yuqing Wang, Bo Zhang, Haibing Ren, Xiaolin Wei, Huaxia Xia, and Chunhua Shen. Twins: Revisiting the design of spatial attention in vision transformers. *Advances in neural information processing systems*, 34:9355–9366, 2021.
- [39] Ilija Radosavovic, Raj Prateek Kosaraju, Ross Girshick, et al. Designing network design spaces. In *Proceedings of the IEEE/CVF Conference on Computer Vision and Pattern Recognition*, pages 10428–10436, 2020.
- [40] Gao Huang, Zhuang Liu, Laurens Van Der Maaten, and Kilian Q Weinberger. Densely connected convolutional networks. In *Proceedings of the IEEE conference on computer vision and pattern recognition*, pages 4700–4708, 2017.
- [41] Ilya O. Tolstikhin et al. Mlp-mixer: An all-mlp architecture for vision. In *NeurIPS*, 2021.

A Appendix

A.1 Experimental Settings

In the experimental configuration of our FViG, we fine-tuned various hyperparameters to enhance performance. The initial learning rate for the FViG was established at $0.3125e-4$, based on the learning rate of $2e-3$ from the ViG model, and tailored to fit our specific hardware configuration and training approach. While the ViG model was run using 8 GPUs and a batch size of 128, our experiments utilized a single GPU with a batch size of 16. As a result, we calculated our learning rate by dividing the ViG’s rate of $2e-3$ by 64 (reflecting the 8 GPUs and the 8 times smaller batch size), to maintain stable training given our more constrained hardware capabilities. Our model completed 100 epochs of training using the AdamW optimizer.

The learning rate followed a cosine schedule, known for promoting efficient convergence. To mitigate overfitting, we applied a dropout rate of 0.1. The architecture of the model featured 12 adjacent nodes and adopted a dynamic dilation rate that escalated with each layer’s depth, increasing by 1 every 4 layers. This method of adaptive dilation allowed the model to perceive a wider range of spatial relationships. Furthermore, the clustering module incorporated 4 multi-heads, improving the model’s capability to synthesize detailed features. Details of these configurations are provided in Table 5. The networks were implemented using PyTorch and trained on a single NVIDIA RTX 3090 GPU.

Table 5: Hyperparameters for FViG

| Hyper-parameters | Value |
|------------------------|------------|
| Batch size | 16 |
| Learning rate | $2e-3/64$ |
| Epochs | 100 |
| Optimizer | AdamW |
| Learning rate schedule | Cosine |
| Dropout rate | 0.1 |
| Adjacent nodes | 12 |
| Dilation rate | 1, 2, 3, 4 |
| Multi-heads | 4 |

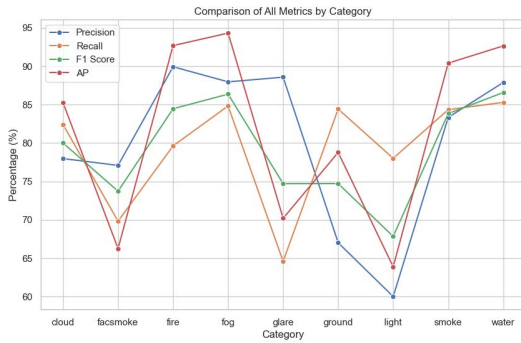


Figure 5: Classification performance metrics of nine categories in the dataset.

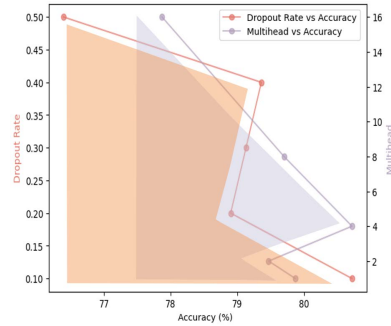


Figure 6: Accuracy of various dropout rate and multihead numbers.

A.2 Classification Results on FDA

In this section, we discuss the classification results obtained in FDA, focusing on performance within nine distinct object categories. For a complete assessment, we examine several metrics per category, such as Precision, Recall, F1 Score, and Average Precision. Additionally, we employ Precision-Recall (P-R) curves and Receiver Operating Characteristic (ROC) curves to visually depict our model’s performance, and we also present confusion matrices to offer an in-depth analysis of the classification precision for each category of flexible objects.

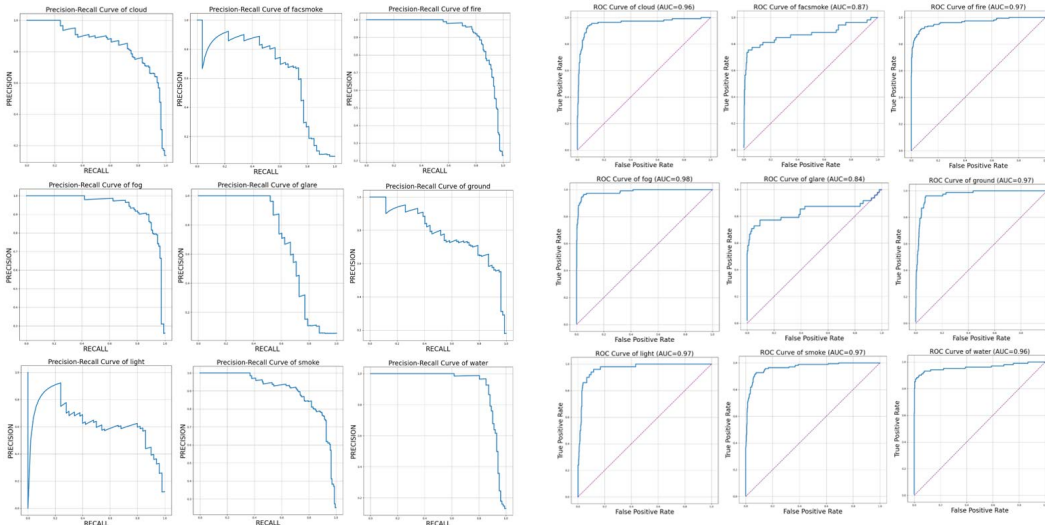


Figure 7: Precision-Recall curves for the classification of nine categories.

Figure 8: ROC curves for the classification of nine categories.

Figure 5 shows that the model achieves high precision, recall, F1 scores, and AP for categories such as cloud, fire, fog, smoke, and water, demonstrating its strong recognition capabilities. However, categories such as ground and light exhibit relatively lower metrics, with precision rates at 67.01% and 60.00%, respectively. Furthermore, the recall rates for facsmoke and glare are 69.81% and 64.58%, respectively. These lower scores may be attributed to the less distinct features of these flexible objects and the higher rate of misclassification caused by small differences between classes. Nevertheless, the overall performance of the model across all categories remains solid, affirming the effectiveness of the proposed FViG model in recognizing flexible objects of various shapes and sizes.

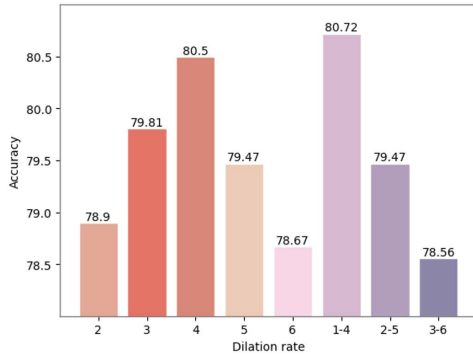


Figure 9: Accuracy of various dilation rate.

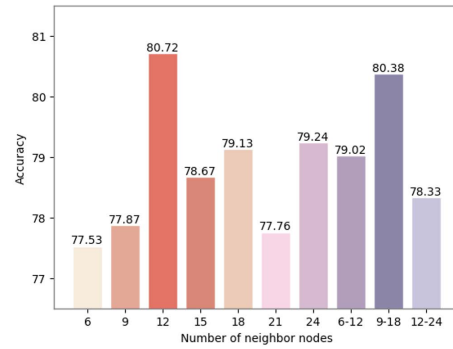


Figure 10: Accuracy of various number of adjacent nodes.

The P-R curve facilitates an understanding of the trade-off between precision and recall at various thresholds. Figure 7 shows the P-R curves for the nine category of objects classified by the FViG. Similarly, the ROC curve demonstrates the relationship between the true positive rate and the false positive rate at various thresholds. The area under the ROC curve (AUC) serves as a comprehensive summary of the model’s performance, with a value of 1 indicating perfect accuracy and a value of 0.5 suggesting no discriminative ability. Figure 8 presents the ROC curves for the nine categories of objects recognized by the FViG. Through the analysis of both P-R and ROC curves, the optimal threshold that achieves a balance between precision and recall can be identified, adapted to the specific needs of the application.

The confusion matrix for the FViG classification in the FDA is depicted in Figure 11. This matrix highlights the performance of the FViG approach in classifying nine categories of flexible objects. Notably, the matrices show remarkable accuracy in recognizing fire and smoke, demonstrating the model’s capability in distinguishing detail features that frequently confuse human perception. Additionally, the model also achieved commendable performance in other categories.

A.3 Comparison of FDA and FireNet datasets

Furthermore, experiments were carried out on the FireNet dataset. As indicated in Table 6, we compared several SOTA techniques, with our FViG consistently outperforming others. However, a trend observed in the experimental results is the unusually high accuracy rates for all SOTA methods tested on the FireNet dataset. This consistent pattern implies that the FireNet dataset lacks the necessary complexity and diversity to adequately test and assess sophisticated object recognition models. Such uniformly excellent results suggest that the dataset fails to accurately reflect the complexity and unpredictability of real-world scenarios, particularly in terms of flexible objects recognition. In comparison, our FDA dataset poses a greater challenge and is more appropriate to push forward research in flexible objects recognition. It encompasses a broader range of scenarios and object types, adding complexities that better replicate the challenges found in real-world settings.

Table 6: Comparison of SOTA Methods and FViG on FireNet Dataset

| Category | Method | Accuracy(%) |
|-------------|---------------------|--------------|
| Transformer | ViT-B/16 [4] | 89.81 |
| | Swin-s [37] | 94.32 |
| | T2T-ViT-14 [34] | 93.63 |
| CNN | Resnet50 [1] | 90.05 |
| | Regnet [39] | 95.94 |
| MLP | Mlp-mixer-base [41] | 93.03 |
| Graph | Coc-small [33] | 98.73 |
| | FViG | 98.85 |

This diversity not only evaluates the performance and adaptability of object recognition algorithms but also fosters the development of more sophisticated and nuanced models capable of handling the intricacies of real-world data. Thus, our FDA dataset serves as a valuable and challenging benchmark that advances and promotes the field of flexible objects recognition.

A.4 Sensitivity Analysis

Furthermore, we carried out experimental investigations to assess the influence of several hyperparameters on the FViG’s performance. These hyperparameters encompass the choice of adjacent node count, the adjustment of the neighboring number, the dilation rate, the dropout ratio, and the multihead count. The results of these experiments are presented in Figure 6, 9 and 10. Based on these results, we ultimately selected a configuration with 12 neighboring nodes ($K=12$), a dilation rate ranging from 2 to 5 ($D = \text{range}(2-5)$), a dropout ratio of 0-0.1, and a multihead count of 4 as our final hyperparameters. With these settings, our FViG achieved its highest accuracy of 80.72%.

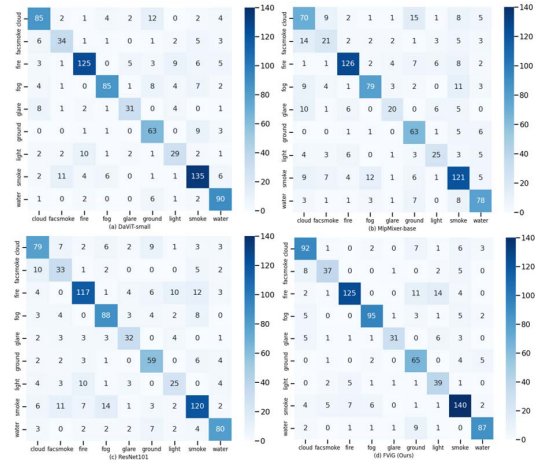


Figure 11: The confusion matrix exhibits the classification performance across various categories. These matrices were derived from four models: a) DaViT-small, b) MlpMixer-base, c) ResNet101, d) FViG.